

Passive control of cylinder aeolian tone by surface protrusions at low Reynolds number

Kusano, Kazuya
Department of Mechanical Engineering, Kyushu University

<https://hdl.handle.net/2324/6788681>

出版情報 : Physics of Fluids. 35 (5), pp.053607-, 2023-05-02. AIP Publishing
バージョン :
権利関係 : © 2023 Author(s). Published under an exclusive license by AIP Publishing.



RESEARCH ARTICLE | MAY 02 2023

Passive control of cylinder aeolian tone by surface protrusions at low Reynolds number

Kusano Kazuya (草野和也) 



Physics of Fluids 35, 053607 (2023)

<https://doi.org/10.1063/5.0146343>



Export
Citation

CrossMark

Articles You May Be Interested In

Rock and roll: Incipient aeolian entrainment of coarse particles

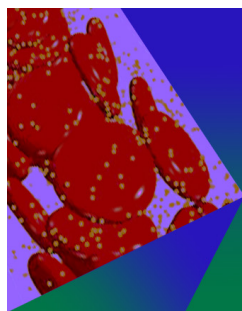
Physics of Fluids (July 2021)

Effects of Wire Resonance on Aeolian Tones

J Acoust Soc Am (July 2005)

Aeolian Tones

J Acoust Soc Am (June 2005)



Physics of Fluids

Special Topic: Flow and Forensics

Submit Today!



Passive control of cylinder aeolian tone by surface protrusions at low Reynolds number

Cite as: Phys. Fluids **35**, 053607 (2023); doi: [10.1063/5.0146343](https://doi.org/10.1063/5.0146343)

Submitted: 13 February 2023 · Accepted: 12 April 2023 ·

Published Online: 2 May 2023




View Online



Export Citation



CrossMark

Kazuya Kusano (草野和也) 

AFFILIATIONS

Department of Mechanical Engineering, Kyushu University, 744 Motooka, Nishi-ku, Fukuoka 819-0395, Japan

^{a)} Author to whom correspondence should be addressed: kusano@mech.kyushu-u.ac.jp

ABSTRACT

Aerodynamic noise control is important for various engineering applications, including automobiles. To develop effective control methods for the flow and sound of bluff bodies, flow past a cylinder is usually studied as a simplified problem. In this study, a passive control technique using surface protrusions was developed to suppress the aeolian tone generated by a two-dimensional laminar flow past a circular cylinder. Protrusions were created on the front and rear surfaces of the cylinder using an optimization approach based on the lattice Boltzmann and adjoint methods, allowing the optimization of complex geometries. The computational results revealed that a pair of protrusions on the front surface could stabilize the separated shear layers by fixing the separation points to their tips, whereas a pair of protrusions on the rear surface can stabilize the separated shear layers by interfering with the interaction between the top and bottom shear layers. Consequently, these shapes effectively suppressed the vortex shedding and aeolian tone while decreasing the mean drag. A shape with symmetrical protrusions on the front and rear surfaces reduced the aeolian tone by 3.6 dB.

Published under an exclusive license by AIP Publishing. <https://doi.org/10.1063/5.0146343>

I. INTRODUCTION

Controlling aerodynamic noise is required in a wide range of engineering applications including turbomachinery and transportation machinery. For automobiles, trains, and aircraft, aerodynamic noise is an important factor that influences the comfort of passengers and neighborhood residents. Particularly, aerodynamic noise is becoming more noticeable in automobiles because of recent electrification. The aerodynamic noise of these vehicles is often associated with bluff bodies, such as the rear-view mirrors of automobiles, pantographs of high-speed trains, and landing gears of aircraft.

To develop effective control methods for the flow and sound of bluff bodies, flow past a cylinder has been intensively studied as a simplified problem in fluid mechanics and aeroacoustics. The fundamental characteristic of the flow past a cylinder is the formation of a von Karman vortex street above a critical Reynolds number. This periodic vortex shedding induces a tonal sound known as the aeolian tone. As discussed in previous review articles,^{1–3} many studies have contributed to the development of control methods for vortex shedding of a cylinder; the control methods are further classified into passive and active controls. The present study focused on passive control, which can be implemented without supplying additional energy to an existing system and at a relatively low cost compared with active control.

Various passive devices, including porous covers,^{4,5} helical cables,^{6,7} hairy flaps,⁸ and longitudinal grooves,⁹ have been proposed to suppress the aeolian tone of a cylinder. Among these, splitter plates have attracted the most attention. The effects of splitter plates on the flow field around a cylinder have been investigated in many experimental^{10–14} and numerical studies.^{15–19} These studies have shown that inserting a splitter plate into the near wake of a cylinder mitigates vortex shedding by disrupting the interaction of the shear layers separated from the top and bottom surfaces.

Furthermore, several studies have investigated the flow and sound fields around a cylinder with splitter plates. Hybrid aeroacoustic simulations based on Lighthill's acoustic analogy have revealed the effects of plate length²⁰ and plate location²¹ on the aeolian tone. Moreover, direct aeroacoustic simulations based on the compressible Navier–Stokes equations have demonstrated the sound control performance of a new splitter configuration, which has a circular arc shape and is concentrically located close to the top and bottom surfaces of a cylinder.^{22,23}

Many of these proposed devices are based on human inspiration and experience and are limited to simple structures and shapes. On the other hand, optimization methods can create more effective control devices with complex shapes. A study has conducted aerodynamic shape optimization using an unsteady adjoint method based on the

incompressible Navier–Stokes equations to minimize the lift oscillation of a cylinder.²⁴ Other studies have conducted aeroacoustic shape optimizations using a hybrid approach to minimize the aeolian tone.^{25,26} However, these studies have modified the entire shape of a cylinder under a small degree of freedom, whereas no study has considered complex shapes, including localized depressions or protrusions, in the shape optimization of a cylinder.

The present study attempted to obtain novel shapes that can effectively control the aeolian tone of a cylinder using aeroacoustic shape optimization. In the optimizations, the degrees of freedom in the shape were sufficiently large to allow the formation of localized depressions or protrusions on the cylinder surface. Such optimizations were realized using the lattice Boltzmann method (LBM) and adjoint method. Furthermore, the sound reduction mechanism of the optimized shapes was investigated.

The remainder of this paper is organized as follows: Section II outlines the numerical methods for aeroacoustic shape optimization. Section III describes the optimization problem and computational conditions. Section IV presents the optimized shapes and simulation results. Finally, the main findings are summarized in Sec. V.

II. NUMERICAL METHOD

A. Lattice Boltzmann method

The flow and acoustic fields were simulated simultaneously using the LBM. The LBM scheme is low dissipative and low dispersive, sufficient for application in direct aeroacoustic simulations.^{27,28} Moreover, it is simple and suitable for parallel computing, allowing unsteady large-scale computations cost-effectively. These features render the LBM a promising approach for computational aeroacoustics for low-Mach-number flows.

The LBM simulates fluid behaviors at the macroscale by computing the streaming and collision processes of a set of particles at the mesoscale. The particle velocity is discretized into a finite number along a regular lattice. In this study, a two-dimensional nine-velocity model (D2Q9) was used along a square lattice. Although D2Q9 is an athermal model, it can reasonably simulate flow-induced sounds under low-Mach-number conditions, assuming that the temperature change is negligible.²⁸

The distribution function of a particle with velocity \mathbf{c}_i at position \mathbf{x} and time t is represented by $f_i(\mathbf{x}, t)$. The evolution of the distribution function is calculated using the lattice Boltzmann equation (LBE) as follows:^{29,30}

$$f_i(\mathbf{x} + \Delta t \mathbf{c}_i, t + \Delta t) = f_i(\mathbf{x}, t) - \frac{1}{\tau} [f_i(\mathbf{x}, t) - f_i^{\text{eq}}(\mathbf{x}, t)], \quad (1)$$

where f_i^{eq} is the local equilibrium distribution function, and τ is the relaxation time. The right-hand side of Eq. (1) expresses the collision operation based on the BGK approximation, which can be computed using only local values at position \mathbf{x} . Moreover, the streaming operation can be completed by simply shifting the distribution function to a neighbor node $\mathbf{x} + \Delta t \mathbf{c}_i$ at the next time step $t + \Delta t$, where the time increment Δt is determined such that the length of vector $\Delta t \mathbf{c}_i$ coincides exactly with the lattice spacing.

In the D2Q9 model, the local equilibrium velocity distribution function f_i^{eq} is given by

$$f_i^{\text{eq}} = w_i \rho \left[1 + \frac{\mathbf{c}_i \cdot \mathbf{u}}{c_s^2} + \frac{(\mathbf{c}_i \cdot \mathbf{u})^2}{4c_s^2} - \frac{\mathbf{u} \cdot \mathbf{u}}{2c_s^2} \right], \quad (2)$$

where ρ and \mathbf{u} denote the density and velocity of the fluid, respectively; w_i is the weighting factor, which is defined as $w_0 = 4/9$, $w_{1-4} = 1/9$, $w_{5-8} = 1/36$; $c_s = c/\sqrt{3}$ is the speed of sound. The relaxation time τ is related to the fluid kinematic viscosity ν as $\tau = 1/2 + \nu/\Delta t c_s^2$.

The fluid density ρ and velocity \mathbf{u} are obtained from the particle velocity moments of the distribution functions, as follows:

$$\rho = \sum_i f_i, \quad \rho \mathbf{u} = \sum_i f_i \mathbf{c}_i. \quad (3)$$

In the athermal models, the fluid pressure is related to the density as $p = \rho c_s^2$.

The interpolated bounce-back (IBB) scheme was used for the wall boundary conditions of complex geometries. It considers boundaries located between grid nodes by interpolating the distribution function on the boundaries based on the bounce-back rule. The linear interpolation scheme proposed by Yu *et al.*³¹ was used. The scheme is expressed as follows:

$$f_i(\mathbf{x}_b, t + \Delta t) = \frac{q_i}{1 + q_i} [\hat{f}_i(\mathbf{x}_b, t) + \hat{f}_{\bar{i}}(\mathbf{x}_b, t)] + \frac{1 - q_i}{1 + q_i} \hat{f}_i(\mathbf{x}_b - \Delta t \mathbf{c}_i, t), \quad (4)$$

where \bar{i} denotes the direction opposite to i , and \hat{f} denotes the distribution function after the collision operation; \mathbf{x}_b is the closest node to the wall in the fluid, and q_i represents the distance between node \mathbf{x}_b and the wall ($0 \leq q_i < \Delta x$). Equation (4) provides the wall boundary condition by linear interpolation using the distribution functions at \mathbf{x}_b and its adjacent node $\mathbf{x}_b - \mathbf{c}_i \Delta t$.

B. Adjoint method

To account for complex geometries, including local protrusions and depressions, shape optimization was performed using the adjoint method. This method can efficiently evaluate the gradients of the objective function with respect to numerous design variables, thereby enabling a high degree of freedom. A discrete adjoint method was used, based on LBE with the IBB condition, which has been proven effective for flow-induced sound problems in the author's previous study.³² This subsection presents an overview of the proposed method.

Shape optimization was used to reduce the flow-induced sounds observed in the far field. Therefore, objective function I was defined as the square mean of the sound pressure in a region during a time window

$$I = \frac{1}{|X_{\text{obs}}| |T_{\text{obs}}|} \sum_{\mathbf{x}_k \in X_{\text{obs}}} \sum_{t_n \in T_{\text{obs}}} \{p(\mathbf{x}_k, t_n) - p_0\}^2, \quad (5)$$

where X_{obs} and T_{obs} indicate a subset of nodes and time steps in which the observation is conducted, respectively; p_0 is the reference pressure, which was the pressure of the uniform flow in this study. Instead of the time-averaged pressure, the constant parameter p_0 was used in Eq. (5) to simplify the calculations. This simplification is reasonable when the observation is conducted in the far field.

The adjoint method considers the governing equations of a fluid as constraint conditions to minimize the objective function. The proposed method is based on the discrete adjoint approach,^{32–34} where the constraint condition for a particle with velocity \mathbf{c}_j ($j = 0, 1, \dots, 8$) at lattice node \mathbf{x}_k ($k = 1, 2, \dots, N_x$) and time step t_n ($n = 1, 2, \dots, N_t$) is expressed as $R_j(\mathbf{x}_k, t_n) = 0$. This condition corresponds to the LBE [Eq. (1)] for inner nodes or the IBB condition [Eq. (4)] for the wall boundary nodes.

To solve the minimization problem with the constraint conditions, Lagrangian J is introduced as follows:

$$J = I + \sum_j \sum_k \sum_n f_j^*(\mathbf{x}_k, t_{n+1}) R_j(\mathbf{x}_k, t_n), \quad (6)$$

where $f_j^*(\mathbf{x}_k, t_{n+1})$ are the adjoint states. The design variables defining object geometries are denoted by α_m ($m = 1, 2, \dots, N_\alpha$). Using the adjoint state f^* , the gradient of objective function I with respect to design variable α_m is given as follows:

$$\begin{aligned} \frac{dI}{d\alpha_m} &= \frac{dJ}{d\alpha_m} = \frac{\partial I}{\partial \alpha_m} + \sum_j \sum_k \sum_n f_j^*(\mathbf{x}_k, t_{n+1}) \frac{\partial R_j(\mathbf{x}_k, t_n)}{\partial \alpha_m} \\ &= \sum_j \sum_k \sum_n f_j^*(\mathbf{x}_k, t_{n+1}) \frac{\partial R_j(\mathbf{x}_k, t_n)}{\partial q_j} \frac{\partial q_j}{\partial \alpha_m}, \end{aligned} \quad (7)$$

where $\partial I / \partial \alpha_m = 0$ is used because the objective function is defined in the far field away from the object. $\partial q_j / \partial \alpha_m$ in Eq. (7) can be numerically calculated at low computational cost. $\partial R_j(\mathbf{x}_k, t_n) / \partial q_j$ in Eq. (7) can be obtained using Eqs. (1) and (4) as follows:

$$\frac{\partial R_j(\mathbf{x}_k, t_n)}{\partial q_j} = \begin{cases} \frac{-1}{(1+q_j)^2} [\hat{f}_j(\mathbf{x}_k, t_n) + \hat{f}_{\bar{j}}(\mathbf{x}_k, t_n)] \\ \quad + \frac{2}{(1+q_j)^2} \hat{f}_j(\mathbf{x}_k - \Delta t \mathbf{c}_j, t_n) & \text{if } \mathbf{x}_k + \Delta t \mathbf{c}_j \notin X_f, \\ 0 & \text{otherwise,} \end{cases} \quad (8)$$

where X_f is a subset of computational nodes whose elements are located in the fluid domain.

At the stationary points of the optimization problem, the adjoint state f^* satisfies the following equation:

$$\begin{aligned} \frac{\partial J}{\partial f_i(\mathbf{x}_{k_0}, t_{n_0})} &= \frac{\partial I}{\partial f_i(\mathbf{x}_{k_0}, t_{n_0})} \\ &+ \sum_j \sum_k \sum_n f_j^*(\mathbf{x}_k, t_{n+1}) \frac{R_j(\mathbf{x}_k, t_n)}{\partial f_i(\mathbf{x}_{k_0}, t_{n_0})} = 0. \end{aligned} \quad (9)$$

Equation (9) provides the adjoint equation, which can be numerically solved to obtain the adjoint state f^* . By substituting f^* into Eq. (7), the gradient of the objective function can be evaluated. The formulation of the adjoint equation and its boundary conditions can be found in the author's previous report.³²

C. Shape optimization method

An aeroacoustic shape optimization method was developed using the LBM and adjoint method. Its flowchart is shown in Fig. 1. First, the flow and acoustic fields were simulated using the LBM for a shape defined by a set of design variables α_m . This direct aeroacoustic

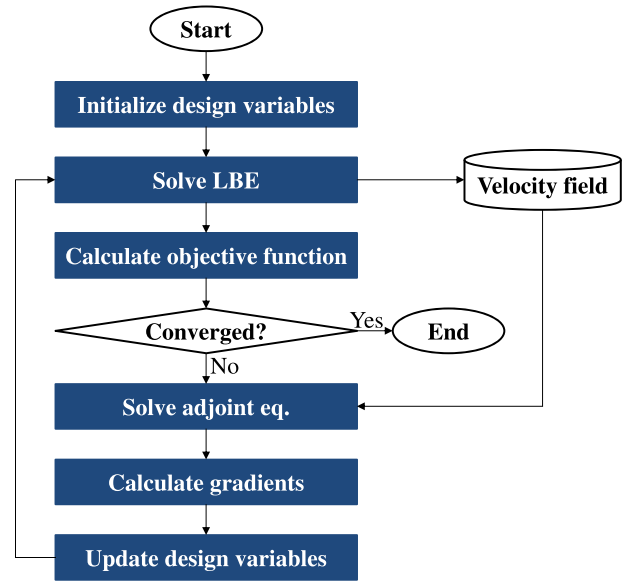


FIG. 1. Flowchart of the shape optimization based on the LBM and adjoint method.

simulation allows the evaluation of objective function I , which is defined as the mean square of sound pressure in the far field during a time window. After the forward analysis, the adjoint equation was computed to calculate the adjoint state f^* . Solving the adjoint equation requires the velocity field data during the time window.^{32,33} The data were provided by the LBM simulation via storage. The gradients of the objective function with respect to the design variables $dI/d\alpha_m$ were evaluated using the adjoint state f^* . Finally, the design variables were updated using the gradient data. These steps were iterated until the objective function converged.

The design variable α_m was updated using the gradient descent method as follows:

$$\alpha_m^{h+1} = \alpha_m^h - \eta \frac{dI}{d\alpha_m}, \quad (10)$$

where superscript h indicates the number of iterations. The step size η was set to $\eta = 0.03D^2/I_0$, where I_0 is the objective function calculated for the initial shape. The optimization processes ended when the following condition was satisfied:

$$\left| \frac{I_h - I_{h-1}}{I_{h-1}} \right| < 10^{-4}, \quad (11)$$

where I_h indicates the objective function evaluated in the h -th iteration.

III. PROBLEM SETUP

A. Flow configuration

The optimization considered a cylinder placed in a uniform flow, where the free-stream velocity was U_∞ . The initial cross-sectional shape of the cylinder was circular with a diameter D . The Reynolds number was defined as $Re = U_\infty D / \nu$.

Although in practical applications, wake flows of bluff bodies are often three-dimensional and turbulent, the unsteady adjoint

calculations are unfeasible for such simulations owing to the large storage requirements. The present study adopted a two-dimensional laminar flow regime to reduce the computational cost and handle the complexity of phenomena and focused on the optimization of the cross-sectional shape. Even at higher Reynolds numbers, the major phenomenon associated with the aeolian tone is regular Karman vortex shedding. Indeed, a tonal component has been clearly observed in the sound spectra for the subcritical flow regime ($Re < 2 \times 10^5$).³⁵ Therefore, shapes developed at a low Reynolds number are expected to be effective at least over the subcritical regime.

In the circular cylinder, laminar vortex shedding was observed in the range of $49 < Re < 194$.³⁶ According to previous numerical studies,^{23,25,37} the condition of $Re = 150$ was adopted, in which periodic vortex shedding was clearly observed. The Mach number of the uniform flow was set to 0.2.

B. Shape parameterization

To suppress the aeolian tone, the cross-sectional shape of the circular cylinder was modified by defining the shape using several parameters. The top and bottom surfaces of the cylinder were constrained to be symmetrical with respect to the streamwise direction to avoid increasing the number of parameters. Figure 2 shows the parameterized shape of the circular cylinder. The origin of the coordinate system was set at its center. The x-axis coincided with the streamwise direction. The shape was expressed using an Akima spline curve.³⁸ The interpolation curve included 21 control points that were equally spaced in the circumferential direction between the two stagnation points in the initial shape.

In contrast to previous optimizations,^{24–26} this study attempted to obtain novel shapes by locally modifying the cylinder surface near the front and rear parts. Three optimization cases with different sets of design variables were considered. In the first case, the first seven control points from the forward stagnation point were variable, and the other points were fixed, as shown in Fig. 2(a). In the second case, the first seven control points from the backward stagnation point were variable, and the other points were fixed, as shown in Fig. 2(b). In the last case, the first seven control points from the forward and backward stagnation points were variable, but the shape was symmetrical with respect to both x- and y-axes.

In these cases, both the circumferential and radial positions of the variable points were modified, except for the control points placed on the stagnation points. For these control points, only the radial position was modified to maintain a symmetrical shape along the x-axis. There were 13 degrees of freedom in all the optimization cases, which is sufficiently large to represent localized depressions or protrusions.

C. Computational conditions

The LBM and adjoint computations were conducted in the domain shown in Fig. 3. The size of the computational domain was $2048D \times 2048D$, and the cylinder was located at its center. As boundary conditions for the outer boundaries, the free-stream density and velocity were specified using the local equilibrium functions. Additionally, to avoid sound reflection from the outer boundaries, a sound-absorbing treatment^{28,32} was applied to the region defined by $r > 768D$, where r is the radial coordinate.

The computational domain was discretized using a hierarchically refined Cartesian grid. Figure 3(a) shows the outlines of the computational grid. The maximum and minimum grid spacings were specified to generate the grid. The maximum grid spacing around the outer boundaries was fixed to $2D$, resolving the wavelength of the aeolian tone with at least 14 grid points. This resolution was previously shown to be sufficient for accurately simulating sound propagations.²⁸

The present study investigated the effect of the minimum grid spacing allocated around the cylinder. Figure 4 shows that the mean drag coefficient $C_{D_{\text{mean}}}$ and amplitude of the lift coefficient fluctuation $C'_{L_{\text{max}}}$ converged on refining the minimum grid spacing Δx_{min} . The relative errors between the second-finest and finest grids were significantly small at 0.49% and 0.98% for $C_{D_{\text{mean}}}$ and $C'_{L_{\text{max}}}$, respectively. Therefore, the second-finest grid ($\Delta x_{\text{min}} = 0.0154D$) was adopted in the shape optimization. The total number of grid points was 6.86×10^6 .

Objective function I was evaluated along the U-shaped observation lines shown in Fig. 3(b). To evaluate the sound pressure level in the far field, the lines were placed $20D$ away from the center of the cylinder. Moreover, to avoid wake flow, no observation line was installed downstream of the cylinder. The observation began after the effect of the initial condition was sufficiently removed. Figure 5 shows the time histories of the lift and drag coefficients in the simulation of the initial shape. The simulation was initiated using the local equilibrium

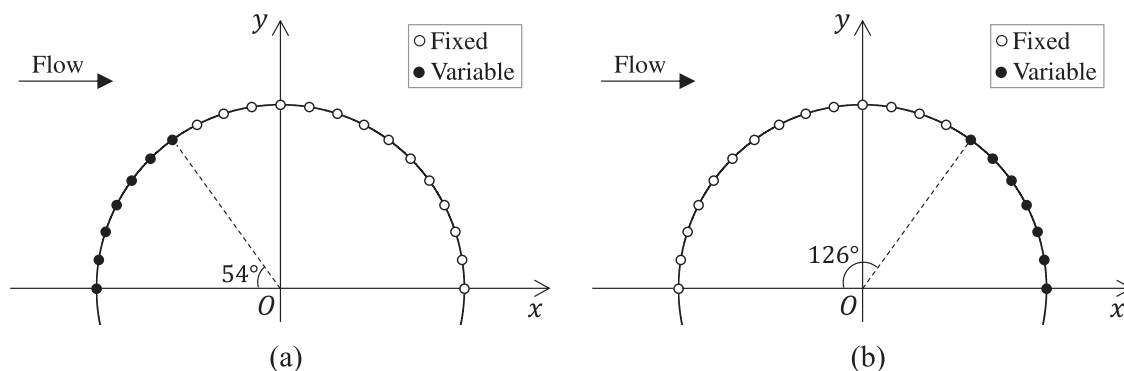


FIG. 2. Cross-sectional shape of the circular cylinder defined using an Akima spline curve with fixed and variable control points for the (a) front and (b) rear surface optimizations.

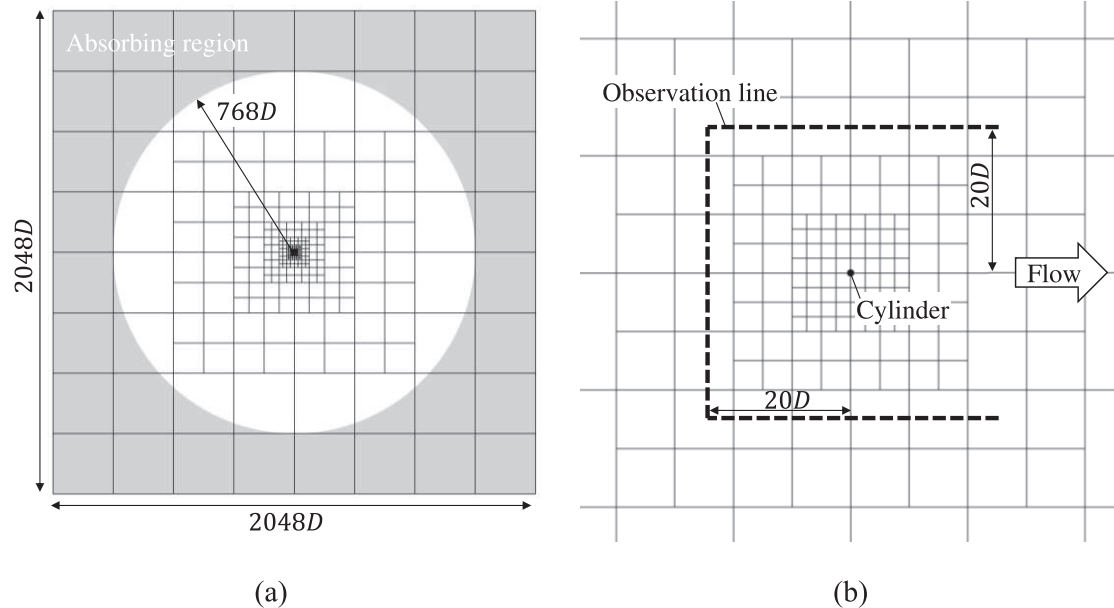


FIG. 3. Computational domain and grid. (a) Overall view; (b) close-up view around the cylinder.

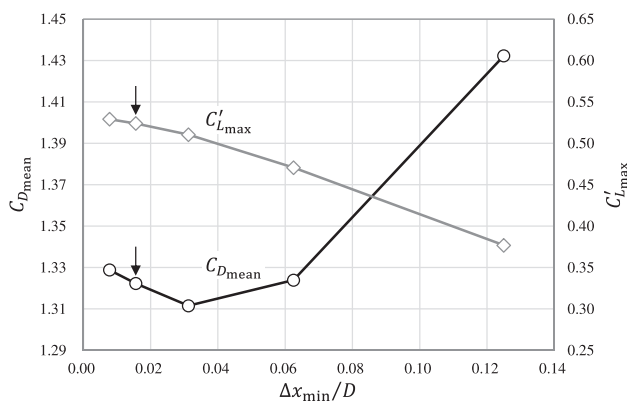


FIG. 4. Mean drag coefficient and amplitude of the lift coefficient fluctuation for different grid spacings. The arrows indicate the grid adopted for the shape optimization.

functions calculated from the free-stream density and velocity. After approximately 150 000 time steps, periodic fluctuations were observed in lift and drag. As shown in Fig. 5, the observations in the LBM simulation and adjoint calculation were performed 50 000 steps after the 250 000th time step. This time window corresponds to 16 cycles of vortex shedding and is sufficient for sound waves to propagate backward from the observation points to the cylinder in the adjoint calculation. The validity of this time window has been shown in a previous report.³² To temporarily store the unsteady velocity field during the time window for the adjoint calculation, high-speed external storage of 5.5 TB was used in this optimization.

IV. RESULTS AND DISCUSSION

A. Validation

The simulation results for the circular cylinder were validated by comparison with the results of other numerical studies.^{23,37,39} As shown in Table I, the drag and lift coefficients and the Strouhal number in the present study were consistent with those in the other studies.

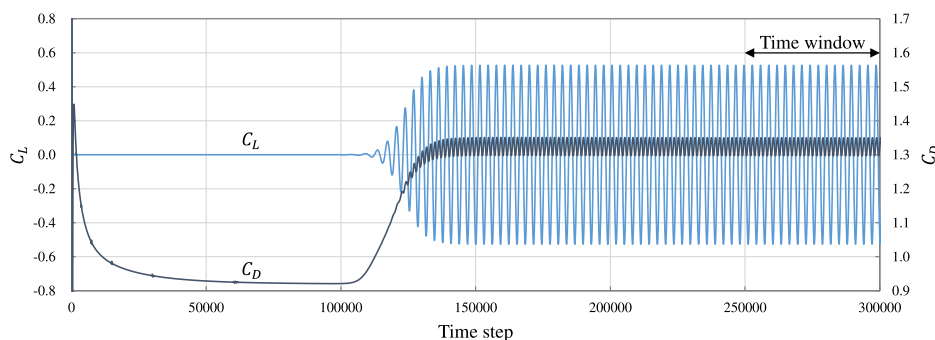


FIG. 5. Time histories of lift and drag coefficients in the simulation of the circular cylinder.

TABLE I. Comparison of the drag and lift coefficients and Strouhal number.

	$C_{D_{\text{mean}}}$	$C'_{D_{\text{rms}}}$	$C'_{L_{\text{rms}}}$	$C'_{L_{\text{max}}}$	S_t
Present	1.32	0.0188	0.373	0.524	0.182
Mahato <i>et al.</i> ²³	1.34	0.0182	0.372	—	0.182
Inoue and Hatakeyama ³⁷	1.34	—	—	0.52	0.183
Shi <i>et al.</i> ³⁹	1.313	—	0.364	—	0.183

Furthermore, Fig. 6 compares the instantaneous distributions of the pressure fluctuation along three radial directions at $t'/T = 0.57$, where time t' is 0 when the lift coefficient is maximum, and T is the period of the lift fluctuation. The azimuth angle θ is defined such that $\theta = 180^\circ$ coincides with the streamwise direction. The figure shows that the present LBM results agreed well with the simulation results by Inoue and Hatakeyama³⁷ based on the compressible Navier–Stokes equations.

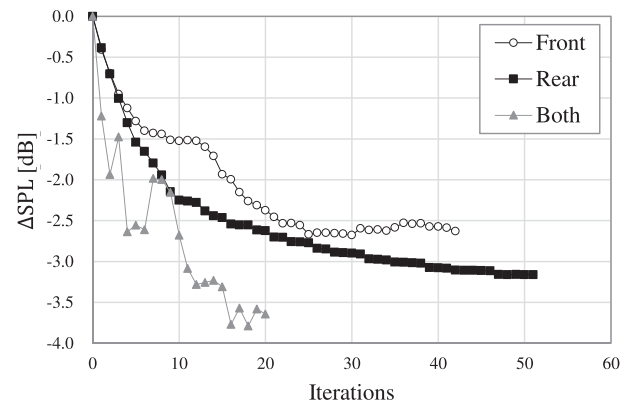
B. Optimized shapes

The sound reduction by the modified shape was evaluated using the sound pressure level difference ΔSPL defined as follows:

$$\Delta\text{SPL} = 10 \log_{10} \frac{I}{I_0} \text{ (dB)}, \quad (12)$$

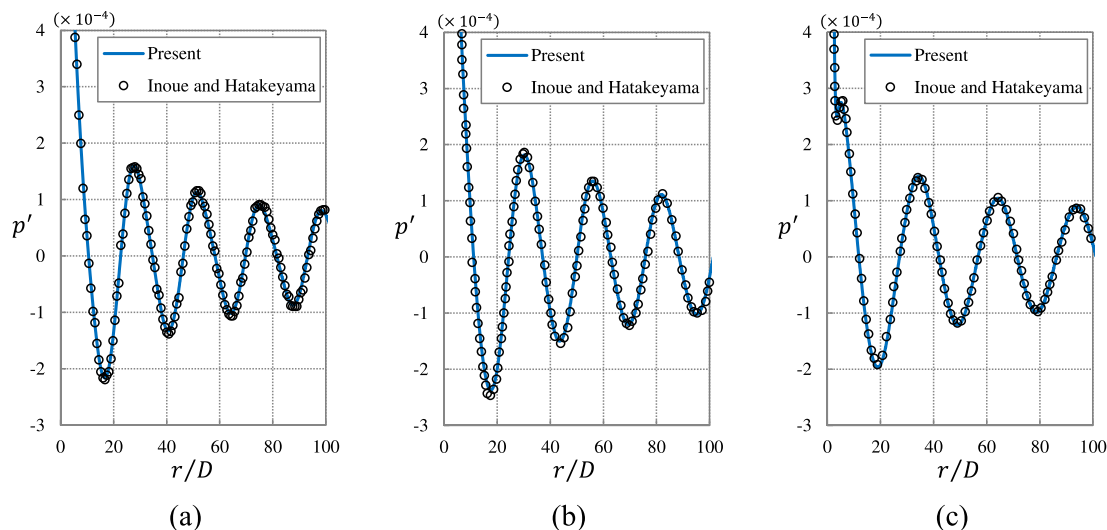
where I_0 is the objective function calculated for the initial shape. Figure 7 shows the histories of ΔSPL in the optimization iterations for the three cases.

Comparing the optimizations for the front and rear surfaces, the sound reduction rates for both were comparable in the first few iterations. Subsequently, the sound reduction rate of the front surface optimization slowed and converged faster than that of the rear surface optimization. Optimizing both surfaces under symmetrical conditions resulted in less sound and faster convergence than optimizing either

**FIG. 7.** Convergence histories of the sound-pressure-level difference in the optimizations.**TABLE II.** Comparison of the mean drag coefficient, RMS of lift coefficient, and Strouhal number between the initial and optimized shapes.

Shape	$C_{D_{\text{mean}}}$	$C'_{L_{\text{rms}}}$	S_t	ΔSPL (dB)
Circular cylinder	1.324	0.373	0.182	0.0
Optimum front surface	1.166	0.181	0.171	−2.6
Optimum rear surface	1.111	0.141	0.179	−3.2
Optimum front and rear surface	0.993	0.066	0.172	−3.6

the front or the rear surface. The results show that ΔSPL decreased almost monotonically when only the rear surface was modified, but occasionally increased in the other two cases that modified the front surface. This is because even slight modifications to the front surface can shift the separation point and significantly alter the flow and sound fields.

**FIG. 6.** Instantaneous distributions of the pressure fluctuation along three radial directions at $t'/T = 0.57$; (a) $\theta = 50^\circ$; (b) $\theta = 78.5^\circ$; (c) $\theta = 120^\circ$.

Each optimization ended when condition (11) was satisfied, and the final shape was considered optimum. As shown in Fig. 7, the optimized front surface reduced the sound pressure level by 2.6 dB compared with the initial shape. A greater sound reduction with $\Delta\text{SPL} = -3.2$ dB was realized by rear surface optimization. Furthermore, optimizing both surfaces under symmetrical conditions resulted in the largest sound reduction of 3.6 dB.

The drag and lift coefficients, and the Strouhal numbers of the initial and optimized shapes are listed in Table II. In low-Mach-number flows, the lift dipole mainly contributes to the generation of the aeolian tone.³⁷ In fact, the root mean square (RMS) values of the lift coefficient for the optimized shapes were significantly lower than those for the circular cylinder. The results indicated that the RMS of the lift fluctuation

was correlated with ΔSPL . Moreover, the mean drag decreased according to sound reduction. The optimized shapes may mitigate the pressure drop downstream of the cylinder by suppressing vortex shedding, resulting in drag reduction. The Strouhal number decreased slightly for the optimized shapes.

Figure 8 shows several modified shapes including the final shape in each optimization, wherein the dotted lines indicate the initial shape. As shown in Fig. 8(a), in the front surface optimization, the first three iterations deformed the front surface to square-like. Furthermore, the corners were extended upstream, and protrusions were observed in the 14th iteration. The protrusions continued to grow further upstream, and their tips reached $x/D = -0.77$ at the final 42nd iteration.

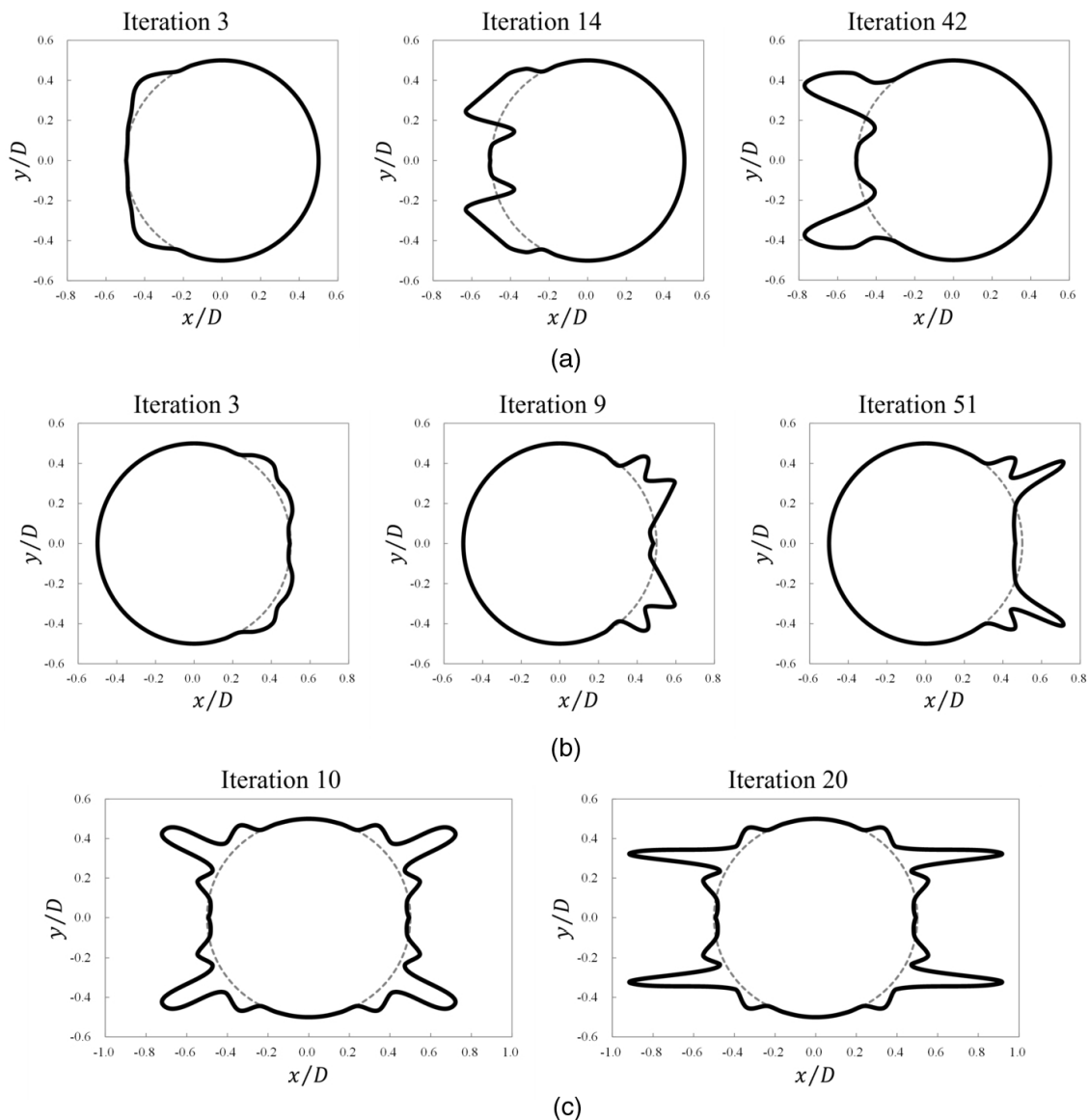


FIG. 8. Shape changes in the optimization for the (a) front surface, (b) rear surface, and (c) front and rear surfaces under symmetry condition.

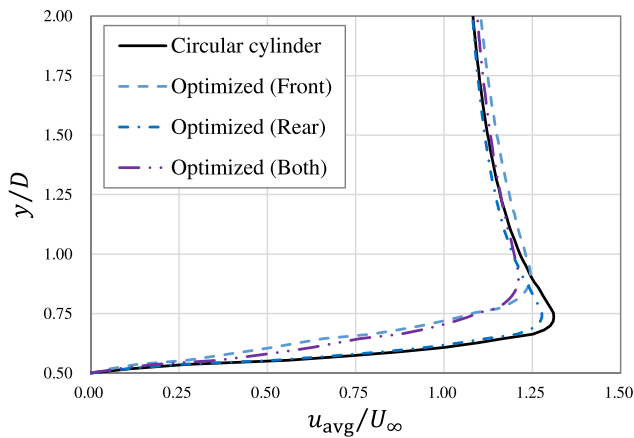


FIG. 9. Time-averaged streamwise velocity profiles at $x/D = 0.0$.

Figure 8(b) shows the shape change in the rear surface optimization. By the third iteration, two small humps were formed on each side of the rear surface. Further, these humps were raised and formed protrusions by the ninth iteration. After this iteration, the protrusions on the upstream side stopped growing. The protrusions on the downstream side were further elongated, finally reaching $x/D = 0.71$.

Figure 8(c) shows the shapes obtained by optimizing the front and rear surfaces under symmetry condition. Only ten iterations of this optimization created long protrusions, which were comparable in size to the protrusions finally obtained in the previous two optimizations. As iterations proceeded, these protrusions were further elongated and inclined to the streamwise direction. The tip of the protrusions reached $x/D = \pm 0.92$ at the final 20th iteration.

The three optimized shapes were characterized by protrusions, which protruded from the front or rear surfaces in the upstream and

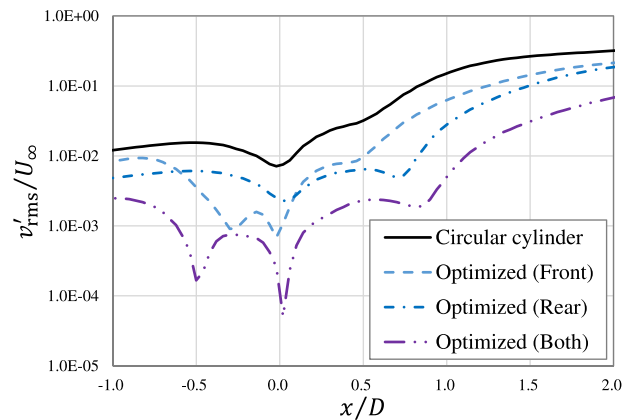


FIG. 10. RMS of the vertical velocity along $y/D = 0.62$.

downstream directions, respectively. These geometries are different from those of previously known passive control devices, such as splitter plates. These results suggest that installing appropriately shaped protrusions on bluff bodies can suppress the aeolian tone while decreasing the mean drag.

C. Flow and acoustic fields

This subsection presents aeroacoustic simulation results to investigate the reduction mechanism of the aeolian tone by the optimized shapes with surface protrusions. First, the time-averaged streamwise velocity profiles along the y -axis were compared between the initial shape and the three optimized shapes, as shown in Fig. 9. The flow over the circular cylinder is accelerated owing to the favorable pressure gradient, and the streamwise velocity is maximum at $y/D = 0.74$.

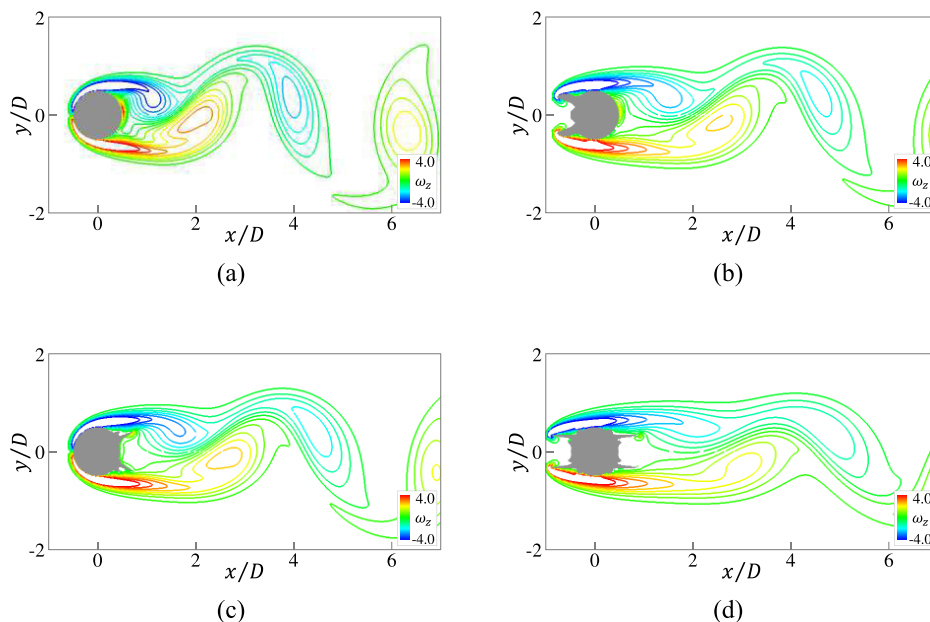


FIG. 11. Instantaneous vorticity contours when the lift coefficient is maximum. (a) Initial shape; (b) optimized front surface; (c) optimized rear surface; (d) optimized front and rear surfaces under the symmetry condition.

Optimizing only the rear surface did not change the velocity profile, except that the peak velocity is slightly smaller. For the other optimized shapes that modified the front surface, the flow acceleration is mitigated compared to the initial shape, and the velocity peak moves to approximately $y/D = 0.9$. These results indicate that optimized front surfaces with protrusions can moderate the velocity gradient around the cylinder.

To compare the oscillation magnitude in the separated shear layer, Fig. 10 shows the RMS of the vertical velocity along $y/D = 0.62$, which was located in the upper separated shear layer. For the initial shape, the vertical velocity fluctuation rapidly increased downstream at $x/D = 0.0$. This rapid increase corresponded to the oscillation of the separated shear layer involved in vortex shedding. A similar increase, starting from $x/D = 0.0$, was observed on the optimized front surface. In this case, the vertical velocity fluctuation was significantly suppressed upstream of $x/D = 0.0$. This may be because the separation point was fixed at the protrusion tip. Consequently, the shear layers in the optimized front surface did not oscillate violently as in the initial shape. The results of the optimized rear surface show that the starting point of the rapid increase in the vertical velocity fluctuation moved downstream to approximately $x/D = 0.71$, which corresponds to the tip location of the protrusions. These results indicate that the protrusions restricted the oscillation of separated shear layers and interfered with the interaction between the two shear layers. For the simultaneously optimized front and rear surfaces under symmetry condition, the vertical velocity fluctuation profile exhibited the above two features observed in the independently optimized front and rear surfaces. As a result, the oscillation in the shear layer was most suppressed by the optimized shape with symmetric protrusions.

Figure 11 shows the instantaneous vorticity contours for the initial and optimized shapes, when the lift coefficient is maximum. Figure 11(a) shows that a vortex was strongly formed from the upper

separated shear layer near the circular cylinder. As shown in Fig. 11(b), the flow was separated at the projection tips, and the vorticity magnitude shed from the separated shear layers was decreased for the optimized front surface according to the moderation of the velocity gradient shown in Fig. 9. Furthermore, the optimized front surface delayed the vortex formation compared to the initial shape because the oscillation of the separated shear layers was mitigated by fixing the separation point at the protrusion tip. Figure 11(c) indicates that the optimized rear surface shifted the location of the vortex formation more downstream than the initial shape and the optimized front surface. In addition, the protrusions on the rear surface interfered with the interaction between the shear layers separated from the top and bottom surfaces like the conventional splitter plates.^{11,15,16,20} However, these optimized protrusions directly restricted the oscillation of the separated shear layers, unlike the conventional splitter plates. These effects of rear surface protrusions resulted in suppressing the oscillation of the shear layers and the delay of the vortex formation. For the shape with symmetrical protrusions on both surfaces, the vortex was formed at the most downstream location among the four shapes, as shown in Fig. 11(d). In addition, this shape most decreased the vorticity magnitude shed into the wake. These may be the result of the combined effect of the front and rear surface protrusions.

The RMS of the pressure fluctuation in the near field is compared in Fig. 12. For the circular cylinder, the highest-pressure fluctuations were observed near $x/D = 1.5$. These pressure fluctuations were caused by the strong vortex shedding, as shown in Fig. 11(a). For the three optimized shapes with protrusions, the pressure fluctuations due to vortex shedding decreased compared to the initial shape [Figs. 12(b)–12(d)]. This is because the oscillation in the shear layers and vorticity magnitude shed from the separated shear layers were decreased by the optimized surface protrusions. Furthermore, the peak locations of the pressure fluctuations shifted downstream according to the delay of vortex formation in the optimized

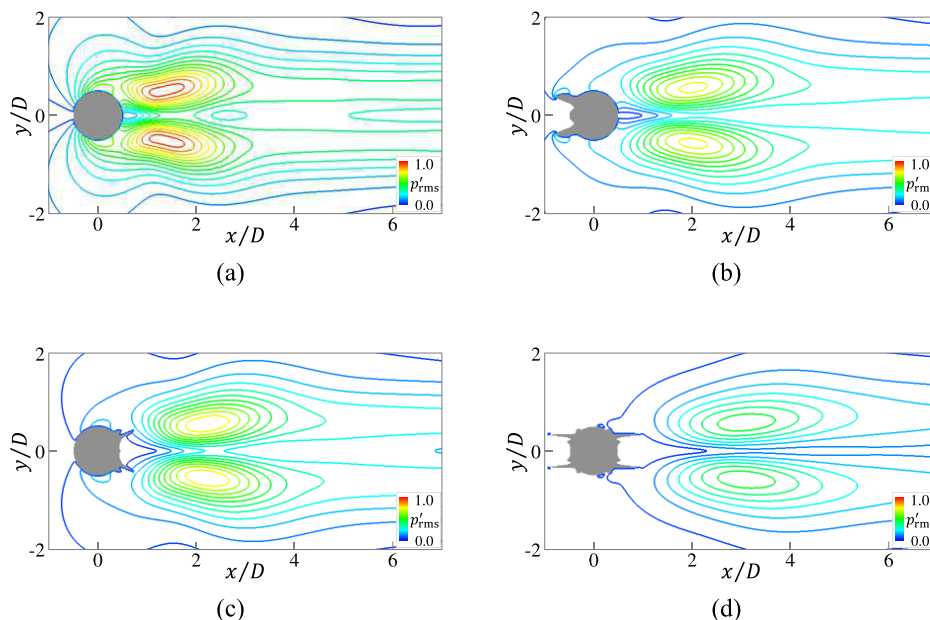


FIG. 12. RMS of pressure fluctuation around the cylinder. (a) Initial shape; (b) optimized front surface; (c) optimized rear surface; (d) optimized front and rear surfaces under the symmetry condition.

shapes. These flow changes contributed to the reduction of the lift fluctuation and the aeolian tone in the optimized shapes, as shown in Table II.

Figure 13 shows the distributions of the instantaneous pressure fluctuation in the far field when the lift coefficient is maximum. The figure reveals that negative and positive pressure fluctuations were alternately radiated from the top and bottom surfaces of the cylinders. A comparison of the acoustic field between the initial and optimized

shapes clearly indicates that these optimized shapes significantly suppressed the generation of the aeolian tone.

Figure 14 shows the power spectral densities of the pressure fluctuations at one of the observation points ($x/D = 0$ and $y/D = 20$). The primary peak in each spectrum correlated with the Strouhal number of the lift fluctuation shown in Table II, indicating the relationship between vortex shedding and the aeolian tone. The results reveal a minor decrease in the tone frequency in the optimized shapes.

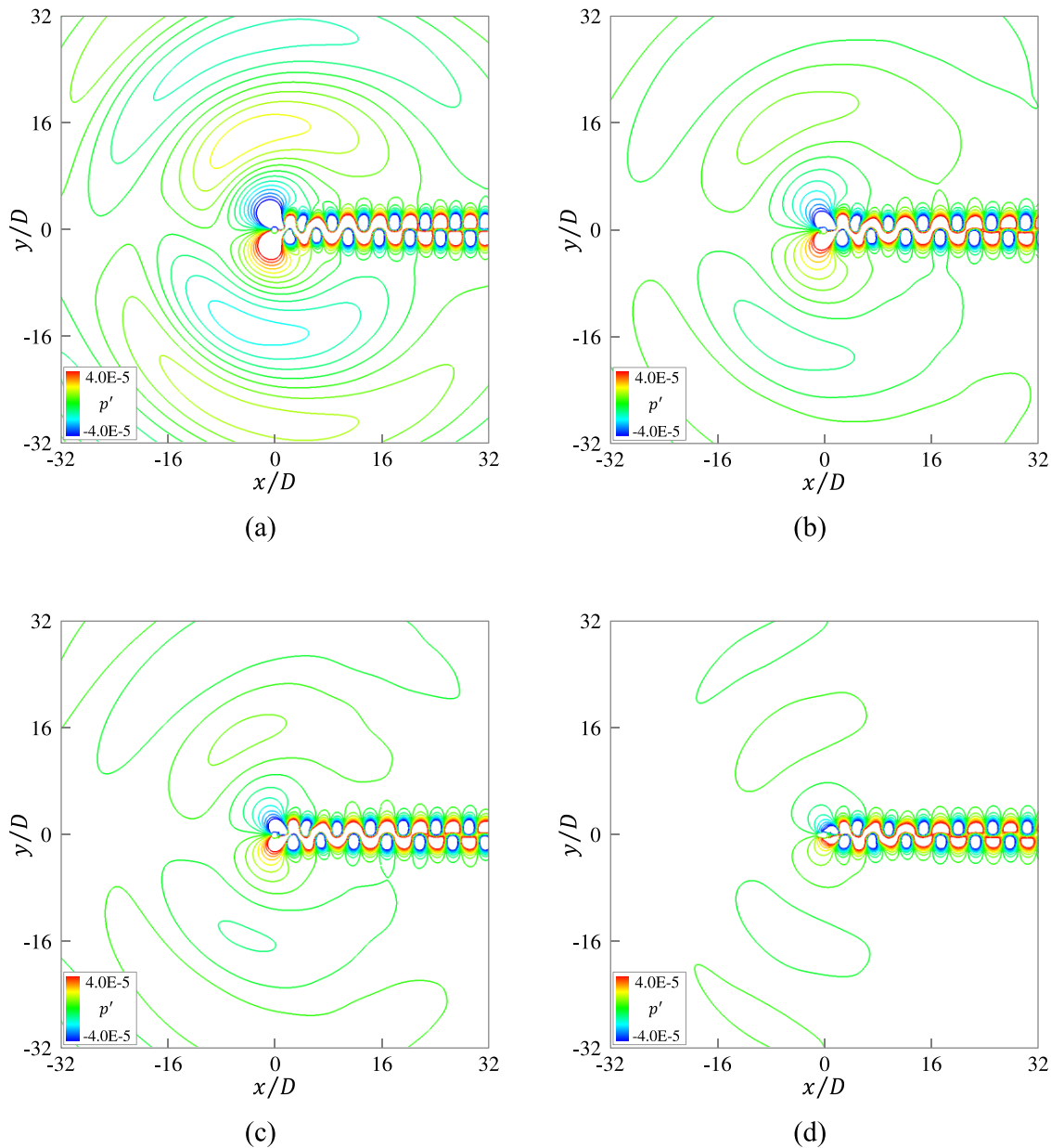


FIG. 13. Instantaneous distributions of pressure fluctuation when the lift coefficient is maximum. (a) Initial shape; (b) optimized front surface; (c) optimized rear surface; (d) optimized front and rear surfaces under the symmetry condition.

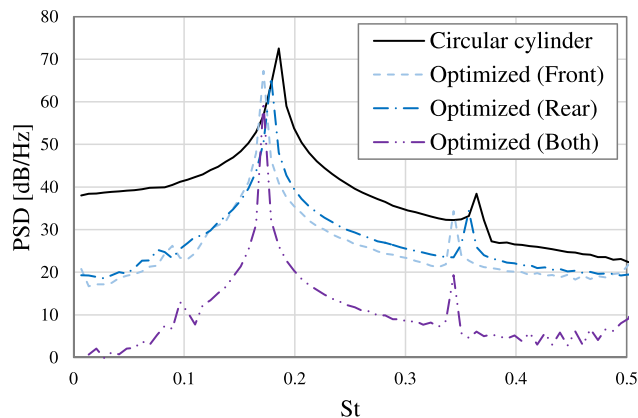


FIG. 14. Power spectral densities (PSDs) of the pressure fluctuation at $x/D = 0$ and $y/D = 20$.

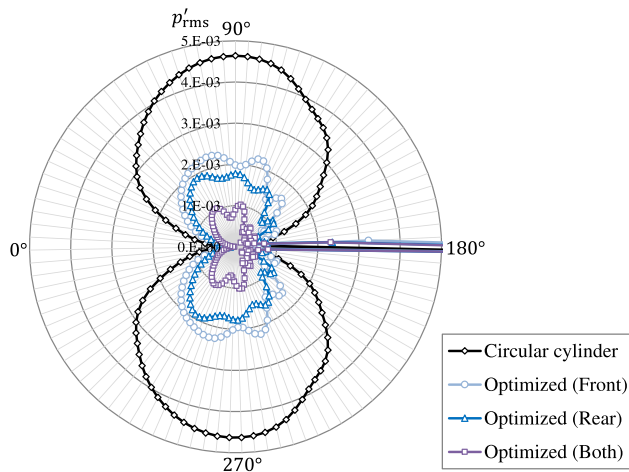


FIG. 15. Polar diagrams of the RMS of the pressure fluctuation at $r/D = 64$.

Finally, the directivity of the aeolian tone was compared between the initial and optimized shapes. Figure 15 shows the RMS of the pressure fluctuation along the circumferential direction at $r/D = 64$. The directivity of the initial shape showed a typical dipole nature dominated by lift fluctuations, whereas the optimized shapes indicate more complex directivity patterns, such as a clover leaf. It appears that the quadrupole sound became recognizable by significantly reducing the lift dipole in the optimized shapes.

V. CONCLUSIONS

New passive control techniques were explored using the aeroacoustic shape optimization method to suppress the aeolian tone generated from a 2D laminar flow past a circular cylinder. The Reynolds and Mach numbers were 150 and 0.2, respectively. In this optimization, the LBM was used for direct aeroacoustic simulations. To update the design variables, the gradients of the objective function with respect to these variables were evaluated using the unsteady adjoint

method. Portions of the cylindrical surface were modified to create local depressions or protrusions.

The optimization results suggested that installing appropriately shaped protrusions on either or both the front and rear surfaces can suppress the aeolian tone while decreasing the mean drag. The shape with symmetrical protrusions on both surfaces realized the greatest reduction of 3.6 dB. The aeroacoustic simulation results revealed that the protrusions on the front surface could stabilize the separated shear layers by fixing the separation points to their tips, whereas the protrusions on the rear surface stabilized the separated shear layers by interfering with the interaction between the top and bottom shear layers.

These findings suggest a new control technique that uses surface protrusions for the flow and sound of bluff bodies. However, further studies are needed to determine whether the proposed method could be effective for high-Reynolds-number flows in engineering applications and whether thin protrusions cause vibrations.

ACKNOWLEDGMENTS

This study was supported by the JSPS KAKENHI (Grant No. JP22K03929). The author gratefully acknowledges research funding from the Harada Memorial Foundation. The computational resources were provided by the Research Institute for Information Technology, Kyushu University.

AUTHOR DECLARATIONS

Conflict of Interest

The author has no conflicts to disclose.

Author Contributions

Kazuya Kusano: Conceptualization (lead); Funding acquisition (lead); Investigation (lead); Methodology (lead); Software (lead); Validation (lead); Visualization (lead); Writing – original draft (lead).

DATA AVAILABILITY

The data that support the findings of this study are available from the corresponding author upon reasonable request.

REFERENCES

- ¹M. M. Zdravkovich, "Review and classification of various aerodynamic and hydrodynamic means for suppressing vortex shedding," *J. Wind Eng. Ind. Aerodyn.* **7**, 145 (1981).
- ²H. Choi, W. P. Jeon, and J. Kim, "Control of flow over a bluff body," *Annu. Rev. Fluid Mech.* **40**, 113 (2008).
- ³S. Rashidi, M. Hayatdavoodi, and J. A. Esfahani, "Vortex shedding suppression and wake control: A review," *Ocean Eng.* **126**, 57 (2016).
- ⁴T. F. Geyer and E. Sarraj, "Circular cylinders with soft porous cover for flow noise reduction," *Exp. Fluids* **57**, 30 (2016).
- ⁵T. F. Geyer, "Experimental evaluation of cylinder vortex shedding noise reduction using porous material," *Exp. Fluids* **61**, 153 (2020).
- ⁶Y. Xing, P. Liu, H. Guo, and L. Li, "Effect of helical cables on cylinder noise control," *Appl. Acoust.* **122**, 152 (2017).
- ⁷L. Li, P. Liu, Y. Xing, and H. Guo, "Experimental investigation on the noise reduction method of helical cables for a circular cylinder and tandem cylinders," *Appl. Acoust.* **152**, 79 (2019).
- ⁸L. Kamps, T. F. Geyer, E. Sarraj, and C. Brücker, "Vortex shedding noise of a cylinder with hairy flaps," *J. Sound Vib.* **388**, 69 (2017).

- ⁹C. Zheng, P. Zhou, S. Zhong, X. Zhang, X. Huang, and R. C. H. So, "An experimental investigation of drag and noise reduction from a circular cylinder using longitudinal grooves," *Phys. Fluids* **33**, 115110 (2021).
- ¹⁰A. Roshko, "On the wake and drag of bluff bodies," *J. Aeronaut. Sci.* **22**, 124 (1955).
- ¹¹E. A. Anderson and A. A. Szewczyk, "Effects of a splitter plate on the near wake of a circular cylinder in 2 and 3-dimensional flow configurations," *Exp. Fluids* **23**, 161 (1997).
- ¹²Y. Jin and L. P. Chamorro, "Passive pitching of splitters in the trailing edge of elliptic cylinders," *J. Fluid Mech.* **826**, 363 (2017).
- ¹³D. Gao, Y. Huang, W. L. Chen, G. Chen, and H. Li, "Control of circular cylinder flow via bilateral splitter plates," *Phys. Fluids* **31**, 057105 (2019).
- ¹⁴Y. Sun, J. Wang, D. Fan, H. Zheng, and Z. Hu, "The roles of rigid splitter plates in flow-induced vibration of a circular cylinder," *Phys. Fluids* **34**, 114114 (2022).
- ¹⁵K. Kwon and H. Choi, "Control of laminar vortex shedding behind a circular cylinder using splitter plates," *Phys. Fluids* **8**, 479 (1996).
- ¹⁶J. Y. Hwang, K. S. Yang, and S. H. Sun, "Reduction of flow-induced forces on a circular cylinder using a detached splitter plate," *Phys. Fluids* **15**, 2433 (2003).
- ¹⁷R. Wang, Y. Bao, D. Zhou, H. Zhu, H. Ping, Z. Han, D. Serson, and H. Xu, "Flow instabilities in the wake of a circular cylinder with parallel dual splitter plates attached," *J. Fluid Mech.* **874**, 299 (2019).
- ¹⁸X. Sun, C. S. Suh, Z.-H. Ye, and B. Yu, "Dynamics of a circular cylinder with an attached splitter plate in laminar flow: A transition from vortex-induced vibration to galloping," *Phys. Fluids* **32**, 027104 (2020).
- ¹⁹M. Zhang, O. Øiseth, and F. Xu, "Laminar flow-induced vibration of a three-degree-of-freedom circular cylinder with an attached splitter plate," *Phys. Fluids* **33**, 113605 (2021).
- ²⁰D. You, H. Choi, M. R. Choi, and S. H. Kang, "Control of flow-induced noise behind a circular cylinder using splitter plates," *AIAA J.* **36**, 1961 (1998).
- ²¹M. S. M. Ali, C. J. Doolan, and V. Wheatley, "Aeolian tones generated by a square cylinder with a detached flat plate," *AIAA J.* **51**, 291 (2013).
- ²²B. Mahato, N. Ganta, and Y. G. Bhumkar, "Mitigation of aerodynamic sound for a laminar flow past a square cylinder using a pair of cowl plates," *Phys. Fluids* **32**, 076108 (2020).
- ²³B. Mahato, N. Ganta, and Y. G. Bhumkar, "Effective control of aeolian tone using a pair of splitter plates," *J. Sound Vib.* **494**, 115906 (2021).
- ²⁴W. Chen, X. Li, and W. Zhang, "Shape optimization to suppress the lift oscillation of flow past a stationary circular cylinder," *Phys. Fluids* **31**, 063604 (2019).
- ²⁵W. J. Gonçalves da Silva Pinto and F. Margnat, "A shape optimization procedure for cylinders aeolian tone," *Comput. Fluids* **182**, 37 (2019).
- ²⁶W. J. Gonçalves da Silva Pinto and F. Margnat, "Shape optimization for the noise induced by the flow over compact bluff bodies," *Comput. Fluids* **198**, 104400 (2020).
- ²⁷S. Marié, D. Ricot, and P. Sagaut, "Comparison between lattice Boltzmann method and Navier–Stokes high order schemes for computational aeroacoustics," *J. Comput. Phys.* **228**, 1056 (2009).
- ²⁸K. Kusano, K. Yamada, and M. Furukawa, "Aeroacoustic simulation of broadband sound generated from low-Mach-number flows using a lattice Boltzmann method," *J. Sound Vib.* **467**, 115044 (2020).
- ²⁹H. Chen, S. Chen, and W. H. Matthaeus, "Recovery of the Navier-Stokes equations using a lattice-gas Boltzmann method," *Phys. Rev. A* **45**, R5339 (1992).
- ³⁰Y. H. Qian, D. D'Humières, and P. Lallemand, "Lattice BGK models for Navier-Stokes equation," *EPL* **17**, 479 (1992).
- ³¹D. Yu, R. Mei, and W. Shyy, "A unified boundary treatment in lattice Boltzmann method," in *Proceedings of 41st Aerospace Science Meeting Exhibition* (AIAA, 2003), Vol. 8, p. 953.
- ³²K. Kusano, "Adjoint sensitivity analysis method based on lattice Boltzmann equation for flow-induced sound problems," *Comput. Fluids* **248**, 105662 (2022).
- ³³E. Vergnault and P. Sagaut, "An adjoint-based lattice Boltzmann method for noise control problems," *J. Comput. Phys.* **276**, 39 (2014).
- ³⁴I. Cheylan, G. Fritz, D. Ricot, and P. Sagaut, "Shape optimization using the adjoint lattice Boltzmann method for aerodynamic applications," *AIAA J.* **57**, 2758 (2019).
- ³⁵N. Alemdaroglu, J. C. Rebillat, and R. Goethals, "An aeroacoustic coherence function method applied to circular cylinder flows," *J. Sound Vib.* **69**, 427 (1980).
- ³⁶C. H. K. Williamson, "Vortex dynamics in the cylinder wake," *Annu. Rev. Fluid Mech.* **28**, 477 (1996).
- ³⁷O. Inoue and N. Hatakeyama, "Sound generation by a two-dimensional circular cylinder in a uniform flow," *J. Fluid Mech.* **471**, 285 (2002).
- ³⁸H. Akima, "A new method of interpolation and smooth curve fitting based on local procedures," *J. ACM* **17**, 589 (1970).
- ³⁹X. Shi, M. Alam, and H. Bai, "Wakes of elliptical cylinders at low Reynolds number," *Int. J. Heat Fluid Flow* **82**, 108553 (2020).